ACS APPLIED MATERIALS & INTERFACES

www.acsami.org

Research Article

# Long-Range Magnetic Order in Oxide Quantum Wells Hosting Two-Dimensional Electron Gases

Jine Zhang,▲ Hui Zhang,▲ Hongrui Zhang,▲ Yang Ma,▲ Xiaobing Chen, Fanqi Meng, Shaojin Qi, Yuansha Chen, Fengxia Hu, Qinghua Zhang, Banggui Liu, Baogen Shen, Weisheng Zhao, Wei Han, and Jirong Sun*

Cite This: *ACS Appl. Mater. Interfaces* 2020, 12, 28775−28782

Read Online

ACCESS | Metrics & More | Article Recommendations | Supporting Information

**ABSTRACT:** To incorporate spintronics functionalities into two-dimensional devices, it is strongly desired to get two-dimensional electron gases (2DEGs) with high spin polarization. Unfortunately, the magnetic characteristics of the typical 2DEG at the $LaAlO_3/SrTiO_3$ interface are very weak due to the nonmagnetic character of $SrTiO_3$ and $LaAlO_3$. While most of the previous works focused on perovskite oxides, here, we extended the exploration for magnetic 2DEG beyond the scope of perovskite combinations, composing 2DEG with $SrTiO_3$ and NaCl-structured EuO that owns a large saturation magnetization and a fairly high Curie temperature. We obtained the 2DEGs that show long-range magnetic order and thus unusual behaviors marked by isotropic butterfly shaped magnetoresistance and remarkable anomalous Hall effect. We found evidence for the presence of more conductive domain walls than elsewhere in the oxide layer where the 2DEG resides. More than that, a relation between interfacial magnetism and carrier density is established. On this basis, the intermediate magnetic states between short-range and long-range ordered states can be achieved. The present work provides guidance for the design of high-performance magnetic 2DEGs.

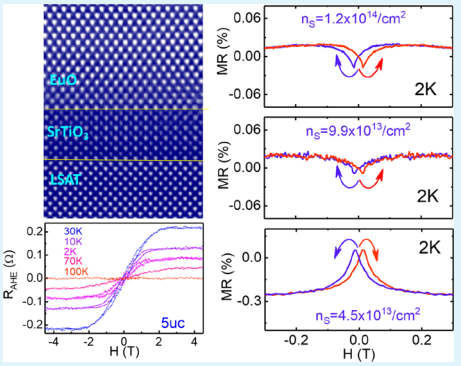


**KEYWORDS:** *magnetic 2DEG, isotropic magnetoresistance, anomalous Hall effect, conductive domain walls, long-range magnetic order*

## 1. INTRODUCTION

Two-dimensional electron gases (2DEGs) at the $LaAlO_3/SrTiO_3$ (LAO/STO) interfaces have received considerable attention due to their exotic properties such as 2D superconductivity,[1,2] 2D magnetism,[3,4] tunable Rashba-typed spin−orbit coupling,[5,6] efficient spin−charge conversion,[7−9] macroscopic quantum effect,[10−14] etc. Among them, the 2D magnetism is of special interest. It provides an opportunity to incorporate spintronics functionalities into 2D oxide devices and therefore is a focus of recent investigations. Unfortunately, the 2D magnetism of the LAO/STO system is extremely weak. Analysis based on X-ray magnetic circular dichroism (XMCD) shows that the magnetization is only in the order of ∼0.01−0.03 $\mu_B$/Ti.[4,15−17] More than that, the long-range magnetic order usually appears at very low temperatures. The highest Curie temperature, deduced from anomalous Hall effects (AHE), is about 10 K,[18] and butterfly shaped magnetoresistance (MR), which is also a fingerprint of ferromagnetic order, emerges at even low temperatures (∼0.3 K).[3]

The weak magnetism of the LAO/STO conducting interface could be ascribed to the nonmagnetic characters of LAO and STO. A question naturally arises: What will happen to 2DEG if the heterostructure is composed of ferromagnetic (ferrimagnetic) perovskite oxides? Since 2DEG resides in STO, there have been attempts to replace LAO with magnetic oxides. As is generally believed, a suitable candidate for LAO should be a polar oxide that allows for a charge transfer to STO. Besides, it should be able to epitaxially grow on STO to form a high-quality interface. $RTiO_3$ (R = La, Nd, Gd, and Sm) is the rare perovskite oxide that simultaneously fulfills these conditions. $GdTiO_3$ (GTO) is ferrimagnetic with a Curie temperature of 32 K, while the other three oxides are antiferromagnetic.[19] By sandwiching STO between two GTO layers, Moetakef et al.[20] obtained a quantum well that showed butterfly shaped MR up to 10 K when the STO layer was 1 nm in thickness; the magnetic proximity effect of GTO on STO makes the latter magnetized. However, the magnetism of the sandwiched STO layer may be weak since AHE was not observed. For the other three antiferromagnetic oxides, the corresponding 2DEGs are not magnetic although sometimes hysteretic MR was observed.[21−23] There have also been attempts to introduce a magnetic buffer layer between LAO and STO. As reported, a 1 $\mu$c thick

Received: March 22, 2020
Accepted: May 27, 2020
Published: May 27, 2020

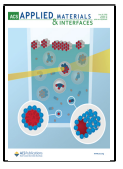

$La_{7/8}Sr_{1/8}MnO_3$ layer greatly improved the mobility of the 2DEG but did not produce visible magnetic effect.[24] A 1 $\mu$c thick $EuTiO_3$ resulted in a sizable AHE.[15] However, it did not increase the temperature span of the AHE; AHE is visible only below 10 K like LAO/STO 2DEG.

From above analyses, it is obvious that the exploration for highly spin-polarized 2DEG is still required. However, the lack of suitable candidates for LAO has greatly impeded the investigations in this regard. While most of the previous works focused on perovskite oxides, recently, we extended the exploration for magnetic 2DEG beyond the scope of perovskite combinations, composing 2DEG with $KTaO_3$ (KTO) and NaCl-structured EuO that is ferromagnetic and owns a high magnetic moment (7 $\mu_B/Eu^{2+}$).[25] We obtained 2DEGs with short-range magnetic order. In this article, we reported on the 2DEG that shows long-range magnetic order and thus unusual behaviors such as isotropic butterfly shaped magnetoresistance and remarkable anomalous Hall effect. More than that, we found the key factor that determines interfacial magnetism. On this basis, we can tune the magnetic states through controlling carrier density.

## 2. EXPERIMENTAL SECTION

STO layers with a thicknesses of $t$ = 5, 10, and 20 $\mu$c were grown on different (001)-oriented $(LaAlO_3)_{0.3}(SrAl_{0.5}Ta_{0.5}O_3)_{0.7}$ (LSAT) single crystal substrates by the technique of pulsed laser deposition. The fluence of the laser pulse was 2 J/cm$^2$, and the repetition rate was 2 Hz (KrF Excimer laser, wavelength = 248 nm). During film deposition, the substrate temperature was maintained at 720 °C and oxygen pressure was fixed to $10^{-5}$ mbar. The resultant films were transferred into a molecular beam epitaxy system for the deposition of a top EuO layer. The base pressure of the system was below $2 \times 10^{-10}$ mbar. Prior to growth, the substrate with the STO cap layer was annealed at 600 °C for 1 h to obtain a clean and well-ordered surface and then cooled down to growth temperature (500 °C). The adsorption-controlled regime was adopted to form a high-quality stoichiometric EuO phase. The deposition rate of Eu was ~8 Å/min, calibrated by a quartz-crystal monitor. The layer thickness was set to 15 nm. The growth process of the EuO film was in situ monitored by reflection high-energy electron diffraction (RHEED). During Eu deposition, the oxygen pressure was maintained at $1.2 \times 10^{-9}$ mbar. A 6 nm thick MgO cap layer was prepared by e-beam evaporation to protect the EuO film from further oxidation when exposed to air.

Ultrasonic wire bonding (Al wires of 20 $\mu$m in diameter) was used for electric contacts. The bonding depth was usually on the order of micrometers. Therefore, the ultrasonic welding will penetrate the insulating MgO/EuO layer to reach the conductive interface for the MgO/EuO/STO/LSAT quantum well. The van der Pauw geometry was adopted for Hall resistance measurements, and the standard four-probe technique was employed for the conventional resistance (including magnetoresistance) measurements. The electrical measurements were performed by a quantum-designed physical property measurement system (PPMS) in the temperature interval from 2 to 300 K and the magnetic field range from 0 to 8 T.

## 3. RESULTS AND DISCUSSION

**3.1. Structural Characteristics of the EuO/STO/LSAT Quantum Well.** Bulk EuO is cubic with a lattice constant of 5.145 Å. LSAT is also cubic with a lattice parameter of 3.868 Å. To get an epitaxial growth on STO or LSAT, the EuO lattice will rotate along [001] axis by 45°.[26] According to the XRD spectra, the EuO layer is nearly cubic with in-plane and out-of-plane lattice constants of 5.15 and 5.14 Å, respectively. Fascinatingly, the large lattice mismatch between EuO and LSAT (5.15 versus 5.47 Å) does not prevent the epitaxial growth of the EuO film, as indicated by the results of RHEED, X-ray diffraction (see Figure S1 for details), and scanning transmission electron microscope with double $C_S$ correctors (STEM, JEOL-ARM200F).

The left panel of Figure 1a is the typical high-angle annular dark-field (HAADF) image of the cross section of EuO/STO(5 $\mu$c)/LSAT, recorded along the [001] zone axis of LSAT. The bright spots in the top layer are the images of the Eu ions. Here, elongated rhombuses along $z$-axis are observed due to the 45° rotation of the EuO lattice with respect to that of STO. This image also shows how the EuO layer is coherently grown on STO, forming a clear interface. The STO layer is 5 $\mu$c in thickness, epitaxially grown on LSAT. Now, two sublattices are observed, corresponding to $Sr^{2+}$ (bright spot) and $Ti^{4+}$ (faint spot) ions, respectively. In Figure 1b we show the electron energy loss spectroscopy (EELS) spectrum images of the Ti-$L_{2,3}$, Eu-$M_5$, and La-$M_{4,5}$ edges, recorded along the vertical line marked in the figure. Both the EuO-STO and STO-LSAT interfaces are very sharp, with negligible interlayer diffusion. These results reveal the high quality of the EuO/STO/LSAT quantum well.

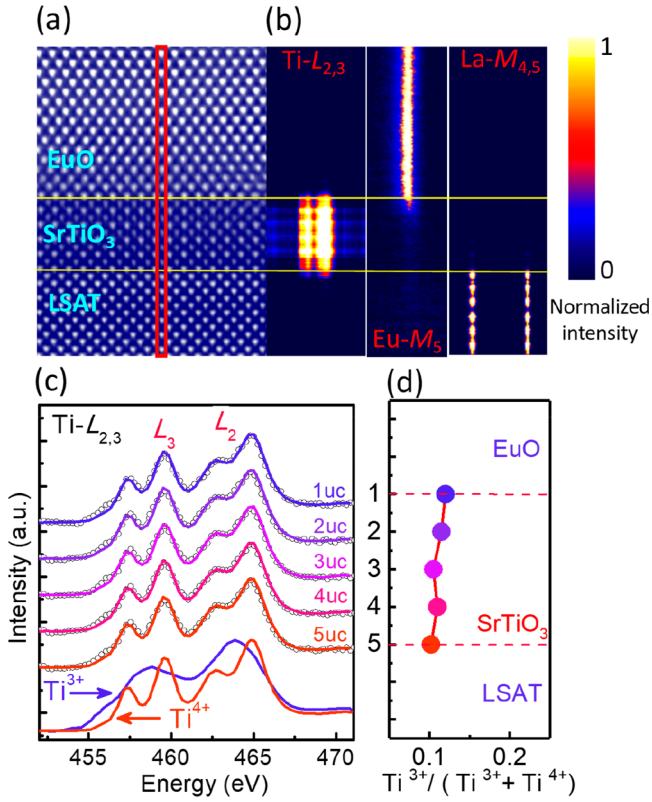


**Figure 1.** (a) High-angle annular dark-field lattice image of the cross section of the EuO/STO(5 $\mu$c)/LSAT quantum well, recorded along the [100] zone axis. For the STO layer, brighter and fainter spots correspond to the Sr and Ti atoms, respectively. For the EuO layer, only Eu atoms are visible. The epitaxial growth of STO on LSAT and EuO on STO can be clearly seen, resulting in two sharp interfaces, as indicated two yellow lines. (b) EELS spectrum images of the Ti-$L_{2,3}$, Eu-$M_5$, and La-$M_{4,5}$ edges, recorded along a vertical column marked in (a). Interlayer diffusion is negligible, which specifies the high quality of the quantum well. (c) Line profiles of the Ti-$L_{2,3}$ EELS spectra. Symbols represent the experimental data, and the solid lines are results of curve fitting based on the two bottom curves that are standard reference spectra of $Ti^{3+}$ and $Ti^{4+}$. For clarity, the EELS spectra of Ti ions have been differently upward shifted. (d) $Ti^{3+}$ content versus distance from the EuO/STO interface.


https://dx.doi.org/10.1021/acsami.0c05332
ACS Appl. Mater. Interfaces 2020, 12, 28775−28782

**3.2. Transport Behaviors of the EuO/STO/LSAT Quantum Well.** To determine the valence state of Ti ions, we performed a quantitative analysis of the EELS spectra. Figure 1c presents the EELS spectra for the Ti ions (symbols) with different distances from the EuO−STO interface. The two solid curves in the bottom of Figure 1c are the standard reference EELS spectra of $Ti^{3+}$ and $Ti^{4+}$, respectively.[27] The above overlaid solid lines are the results of multiple linear least-squares fitting, derived from a weighted linear combination of the $Ti^{3+}$ and $Ti^{4+}$ reference spectra.[27−30] On the basis of this analysis, the content of $Ti^{3+}$ can be obtained. It is ∼11%, essentially independent of the distance from interface (Figure 1d). This means that the STO layer has been uniformly electron doped by the oxygen vacancies generated in the growth process of EuO. If all doped electrons are mobile, the carrier density ($n_S$) of the 2DEG will be ∼$3.6 \times 10^{14}$ $cm^{-2}$.

Figure 2a shows the sheet resistance ($R_S$) of the EuO/STO/LSAT quantum well as a function of temperature ($T$). The transport behaviors are essentially metallic. The resistance decreases monotonically as the sample is cooled from 300 down to 50 K. As for the slight resistance upturn below 50 K, it is an effect of Kondo scattering. As an example, we calculated the Kondo effect for sample $t$ = 10 $\mu$c adopting the zero-field generalized Hamann expression and found that the calculated results reproduced the experimental data very well (symbols in Figure 2a). Please refer to Figure S2 for detailed calculations. From 5 to 20 $\mu$c samples, the whole $R_S-T$ curve exhibits a downward shift. This can be ascribed to the increase of the conductive layer thickness, which leads to an increased number of charge carriers. The carrier density of the quantum well is shown in Figure 2b. It is ∼$2.3 \times 10^{14}$ $cm^{-2}$ at 300 K for sample $t$ = 5 $\mu$c, lower than the value deduced from the EELS analysis (∼$3.6 \times 10^{14}$ $cm^{-2}$). Obviously, considerable charge carriers are localized.[31] This is because the electron energy loss spectroscopy (EELS) is sensitive to both mobile and nonmobile carriers, whereas the transport measurements are only sensitive to the former.[31] With the decrease of temperature, carrier density displays a smooth decease. For 5 and 10 $\mu$c samples, a downward bending can be seen in the $n_S-T$ relation below 40 K (marked by an arrow), corresponding to the enhancement of the Kondo effect. A further analysis shows that $n_S$ is nearly proportional to the width of the quantum well. It means that the STO layer has been uniformly reduced by EuO to the same degree though the layer thickness is different.

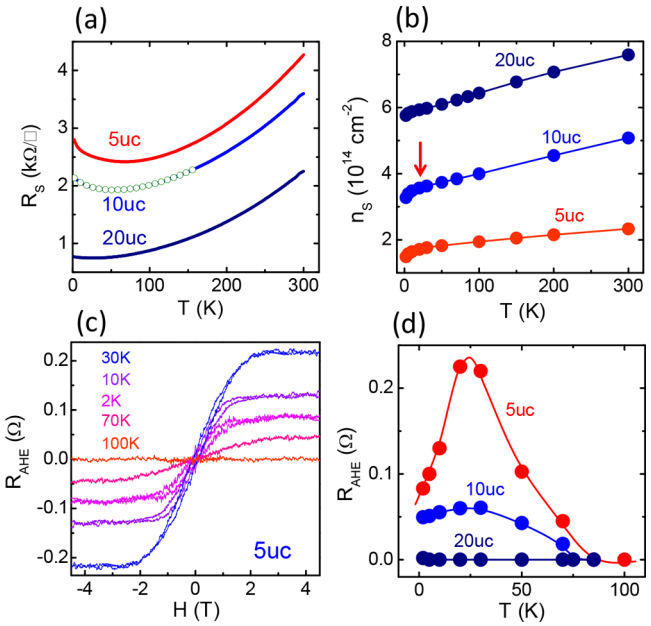


**Figure 2.** (a) Sheet resistance as a function of temperature for EuO/STO/LSAT quantum well. The upturn below 70 K stems from Kondo scattering, obtained with van der Pauw technique. (b) Carrier density of the EuO/STO/LSAT quantum well, presented as a function of temperature. A gradual freezing out of the charge carrier was observed with the decrease of temperature. (c) Hall resistance as a function of magnetic field, with the linear component has been subtracted. Stepwise $R_{xy}-H$ dependence is observed, indicating the occurrence of anomalous Hall effect. (d) Anomalous Hall resistance as a function of temperatures. It shows first a rapid and then a slow decrease upon cooling. The maximal AHE appears at ∼25 K.

For a control experiment, we also fabricated the EuO layer on LSAT under the same conditions as those for the EuO/STO/LSAT quantum well and found that the resistance was beyond the scope of our measuring system in the whole temperature range investigated. This result indicates that oxygen deficiency in EuO, if it exists, is not high enough to drive EuO into a conducting state.

Since the discovery of LAO/STO 2DEG, people have been exploring the STO-based 2DEG caused by other typical oxides ($\gamma$-$Al_2O_3$/$SrTiO_3$,[32] $GdTiO_3$/STO/$GdTiO_3$[20]). The study of EuO/STO/LSAT 2DEG provides a new space for exploring the STO-based 2DEG.

**3.3. Long-Range Magnetic Order of the EuO/STO/LSAT Quantum Well.** The quantum well exhibits magnetic characters, as indicated by the appearance of definite AHE. Figure 2c illustrates the anomalous Hall resistance ($R_{AHE}$) of the 5 $\mu$c sample, as a function of perpendicular magnetic field ($H$), where the linear background has been corrected. With the increase of magnetic field, the Hall resistance first grows rapidly and then, above a threshold field, saturates to a constant value. A close view of the $R_{AHE}-H$ curves shows the occurrence of magnetic hysteresis around $H$ = 0. These are typical features of AHE. Figure 2d displays the temperature dependence of the saturation $R_{AHE}$. According to Figure 2d, $R_{AHE}$ emerges at 70 K, increases rapidly with the decrease of temperature, and gains the maximal value at ∼25 K. After that, a crossover from the increase to decrease appears, due to enhanced Kondo effect. As is well established, AHE is a fingerprint of magnetic order, which can be either long or short range. Noting the fact that 70 K is exactly the Curie temperature of the EuO film (see Figure S3 for the magnetic properties of EuO film), the magnetism of the STO layer may have a close relation to EuO. Notably, AHE was not observed in GTO/STO/GTO.[20] It means that the magnetic character of our 2DEG is strong compared with GTO/STO/GTO.

AHE was also observed in the 10 $\mu$c sample, though the $R_{AHE}$ values were significantly depressed. For the 20 $\mu$c sample, no reliable AHE was identified. Apparently, the magnetic order in STO prefers to appear in the proximity of the EuO/STO interface and is a proximity effect of EuO on STO.

In addition to AHE, magnetic hysteresis is also a fingerprint of magnetic order. Figure 3a illustrates the MR of EuO/STO(5 $\mu$c)/LSAT, obtained in a parallel field. Butterfly shaped MR appears when the cycling magnetic field is between ±0.1 T, leading to two resistance dips, where $H_C$ is the coercive field of the EuO film, as will be seen later. This result suggests the establishment of a magnetic order in the STO layer where the 2DEG resides.[33,34] The magnetic order should be long range in


https://dx.doi.org/10.1021/acsami.0c05332
ACS Appl. Mater. Interfaces 2020, 12, 28775−28782

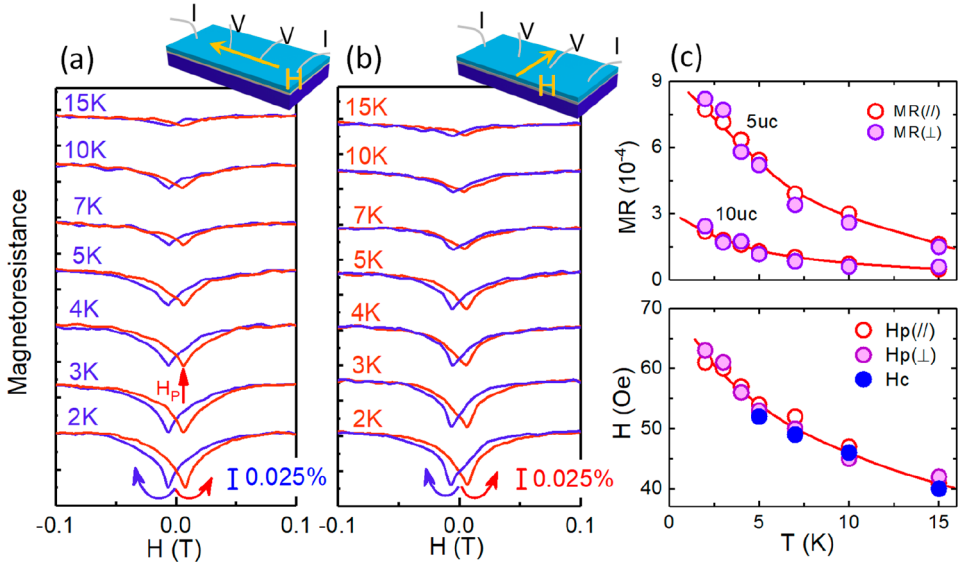


**Figure 3.** (a and b) Magnetoresistance measured in the in-plane field (a) parallel or (b) perpendicular to applied current for the EuO/STO(5 $\mu$c)/LSAT quantum well, obtained by the four-probe technique. Sketches in (a) and (b) show the corresponding experiment setups. Magnetic hysteresis appears while cycling magnetic field along the path +0.1 T to −0.1 T and to +0.1 T, indicating the emergence of magnetic order in STO. Results obtained at different temperatures were upward shifted for clarity. Arrows mark the direction of magnetic sweeping. (c) Summary of the magnetoresistance of different samples (upper panel) and the comparison of the coercive field of EuO ($H_C$) and the character field for magnetoresistance minimum ($H_P$, bottom panel). Both parallel and perpendicular MR and $H_P$ values are presented, respectively represented by red and purple symbols. Solid lines are guides for the eye.

nature[33,34] since a short-range order will never give rise to MR−$H$ curves with two dips at $\pm H_C$ regardless of the direction of the in-plane field. In fact, a short-range order always causes two MR peaks at $\pm H_C$.[25,35]

Here, short-range magnetic order means magnetic state with isolated magnetic clusters dispersed in nonmagnetic (or paramagnetic) background. A typical short-range order appears in the intermediate state between the paramagnetic and ferromagnetic state, as shown in ref 36. Magnetic granular film is a special short-range ordered system.[35] In contrast, a long-range order is a magnetic state in which all magnetic moments are strongly coupled and form an ordered arrangement. The typical system is $La_{2/3}Sr_{1/3}MnO_3$ film at low temperatures.[37]

Hysteretic MR marked with two MR dips suggests the formation of magnetic domains in the STO layer where the 2DEG resides[33,34] (Figure 3a). Magnetic hysteresis is a consequence of field-induced reluctant rearrangement of magnetic domains. In a word, AHE indicates the appearance of magnetic order while hysteretic MR specifies the long-range character of the magnetic order. The magnetic hysteresis emerges at 15 K and enhances upon further cooling; it has been promoted from ∼0.3 K for LAO/STO to ∼15 K for the present sample.

An interesting observation is that the MR is isotropic, i.e., the MR−$H$ curves obtained with parallel and perpendicular fields are identical (Figure 3a,b). This is different from the conventional anisotropic MR, for which MR peaks and MR dips emerge along two orthogonal field directions.[34] As will be seen later, isotropic MR is an indication of the appearance of conductive domain walls in STO.

In the upper panel of Figure 3c, we show the MR as a function of temperature (see Figure S4 for the determination of butterfly shaped MR values). The MR of te 5 $\mu$c sample is higher by a factor of 3.5 than that of the 10 $\mu$c sample. It is invisible for the 20 $\mu$c sample (not shown). This result confirms the inference of the AHE, i.e., the 2D magnetism is an interfacial effect. The bottom panel of Figure 3c shows the character field corresponding to MR minima ($H_P$), obtained from Figure 3a,b. For comparison, the coercive fields of the EuO film ($H_C$) are also included (refer to Figure S3 for the magnetic behavior of the EuO film). Remarkably, three sets of data collapse onto the same master curve. This result indicates that the resistance minima appear when magnetic domains are most randomly orientated. This in turn leads to an inference that the domain walls of STO are more conductive than elsewhere. In this picture, MR dips should locate at coercive field where the most domain walls form. Obviously, isotropic MR is a unique feature of the present 2DEG with a long-range magnetic order.

At present, we only have a primary explanation to this phenomenon: charge carriers may tend to accumulate at domain walls, making the latter more conductive than elsewhere. There are reports showing that STO oxygen vacancies prefer to concentrate on the boundaries between crystal domains.[38] If magnetoelastic coupling of the magnetized STO layer is strong enough, the rearrangement of magnetic domains may induce structural deformation, leading to additional crystal domain boundaries and thus depressed resistance.

### 3.4. Magnetic Ordered Tuned by Carrier Density.

According to previous and present works, sometimes the magnetic order of the 2DEG is short range[25] and sometimes it is long range. A further issue to be addressed is the key factors affecting magnetic order. For the LAO/STO system, there are reports that the magnetic coupling between local moments is generated by a RKKY-like exchange.[39] This means a close relation between magnetic interaction and carrier density.[40] Unfortunately, it is difficult to control the carrier density of EuO/STO/LSAT since STO is always over reduced by EuO to a definite degree in the suitable temperature range for the growth of EuO. As an alternative, we prepared EuO/$KTaO_3$ (EuO/KTO) quantum wells with different carrier densities. KTO and


https://dx.doi.org/10.1021/acsami.0c05332
ACS Appl. Mater. Interfaces 2020, 12, 28775−28782

STO are quite similar in many aspects. First, both oxides exhibit quantum paraelectricity and have a high dielectric constant, which is a prerequisite for obtaining high mobility 2DEG. Second, they are the only perovskite oxides from which 2DEG can be obtained when capped with an appropriate oxide layer such as $LaAlO_3$.[41,42]

The samples were fabricated by capping an EuO layer of 15 nm on KTO while keeping substrate at a temperature between 400 and 550 °C. In general, increasing the deposition temperature will enhance the outward diffusion of oxygen from STO to EuO, resulting in an increased carrier density. As confirmed by the experiment of Hall effect, samples obtained by tuning the substrate temperature have the carrier densities ranging from ~$4.5 \times 10^{13}$ (obtained at 400 °C) to ~$1.2 \times 10^{14}$ $cm^{-2}$ (obtained at 550 °C) at 2 K.

Remarkably, hysteretic MR of EuO/KTO mimicking that of EuO/STO/LSAT was observed when $n_S$ was high (top panel of Figure 4a), confirming the establishment of a long-range

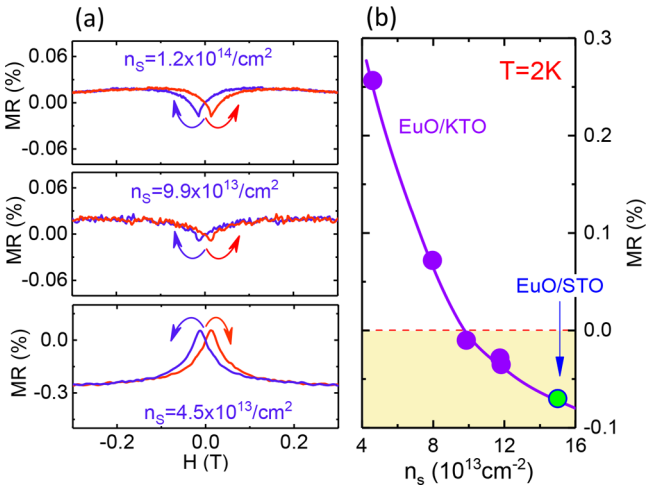


**Figure 4.** (a) Magnetoresistance measured in parallel magnetic field for the EuO/KTO 2DEGs with different carrier densities, obtained at 2 K. From bottom to top panels, the carrier density increases from $4.5 \times 10^{13}$ to $1.2 \times 10^{14}$ $cm^{-2}$. Arrows mark the direction of magnetic cycling. (b) Peak values of the MR as a function of carrier density. The result of EuO/STO(5 $\mu c$)/LSAT is also presented for comparison. Data of 10 and 20 $\mu c$ samples are not shown here since the interfacial effect in these two samples have been significantly shunted by interior layers.

magnetic order in KTO. With the decrease of the carrier density, MR first decreases in magnitude and then, fascinatingly, reverses its sign when $n_S$ is lower than $10^{14}$ $cm^{-2}$, showing two maxima in the MR−$H$ curve (middle and bottom panels of Figure 4a). Notably, two MR maxima have been reported before for the EuO/KTO 2DEG with $n_S \approx 8 \times 10^{13}$ $cm^{-2}$.[25] As evidenced, in that case, isolated magnetic clusters dominate the magnetic structure of the interfacial layer of KTO, resulting in MR behaviors similar to that of magnetic granular film.[35] Obviously, the magnetic order in quantum well undergoes a long-to-short-range evolution as the carrier density decreases. The peak values of MR are shown in Figure 4b as a function of $n_S$. The result of EuO/STO(5 $\mu c$)/LSAT is also presented for comparison. Theoretically speaking, any intermediate magnetic state can be obtained by carefully tuning the carrier density.

On the basis of a simple analysis, we can understand the strong dependence of magnetic order on carrier density. When $n_S$ is low, the magnetic exchange will be weak,[40] and, as a consequence, the magnetic order is imperfect. This explains the appearance of magnetic clusters. With the increase of the carrier density, magnetic coupling is enhanced. As a result, the induced magnetic order near the interface can be efficiently delivered to the inner KTO layers. This in turn causes an expansion of magnetic clusters, resulting in a long-range magnetic order. Due to the similarities of STO and KTO in many aspects, a similar process is expected in the STO-based quantum well if the carrier density there can be controlled.

**Picture for the Magnetic Structure in Quantum Wells.** So far, our investigation on MR has been limited to low fields. Extending to a high field range, a distinct background MR emerges. Figure 5 shows the MR of EuO/STO(5 $\mu c$)/LSAT and EuO/STO(20 $\mu c$)/LSAT. The data for a typical EuO/KTO quantum well ($n_S = 8 \times 10^{13}$ $cm^{-2}$) are also included for comparison. In addition to the butterfly shaped MR around $H$ = 0, a bell shaped background appears for EuO/KTO and EuO/STO(5 $\mu c$)/LSAT. Different from the low field one, this background MR is reversible for magnetic cycling and persists up to high fields. We found that the Khosla and Fischer formula[43−46] provides a good description for the background MR (dashed lines in Figure 5)

$$\mathrm{MR} = -a^2 \ln(1 + b^2 H^2) \quad (1)$$

adopting suitable parameters of $a$ and $b$ (see Figure S5 for detailed calculations). Obviously, the background MR stems from the depression of the scattering from isolated magnetic moments. It is the presence of these randomly oriented local moments that causes the Kondo effect in EuO/KTO and EuO/STO(5 $\mu c$)/LSAT (refer to Figure S6 for the resistive behavior of EuO/KTO). For the 20 $\mu c$ sample without showing Kondo effect, the background MR is slightly positive, due to the shrinkage of electron wave function in magnetic field (Figure 5c).[47]

Based on the above analyses, we can get a sketch for the magnetic structure of the interfacial layer. Parts a and b of Figure 6 are plane views of the interfacial layers of KTO(STO). As shown in Figure 6a, magnetic clusters form when carrier density is low, dispersing in a background that owns isolated magnetic moments. Depression of the spin scattering from magnetic clusters results in a hysteretic MR. In this case, MR shows two peaks at coercive field. In addition to magnetic clusters, localized magnetic moments in the background will also cause spin scattering, resulting in the Kondo effect. The background MR is a consequence of the alignment of randomly directed magnetic moments. It is thus reversible for magnetic cycling. With the increase of carrier density, magnetic clusters expand and merger with each other, forming connected magnetic domains (Figure 6b). The rearrangement of magnetic domain gives rise to butterfly shaped MR characterized by two dips at coercive field. Meanwhile, the background MR remains visible because of presence of isolated magnetic moments in the background, which will give rise to Kondo scattering.

On the basis of density-functional theory calculations, we investigated the magnetic characteristics of the STO layer and found a ferromagnetic ground state (see Figure S7 for detailed results). Further analysis reveals how the proximity effect of EuO on STO takes place: Due to structural relaxation at interface, Eu 5d states are partially occupied and polarized by Eu 4f electrons. This in turn causes a spin polarization of Ti 3d electrons, whose wave function has an overlap with that of Eu 5d electrons. In general, some of the Ti 3d electrons will be localized due to interfacial scattering, forming localized magnetic moments. As


https://dx.doi.org/10.1021/acsami.0c05332
ACS Appl. Mater. Interfaces 2020, 12, 28775−28782

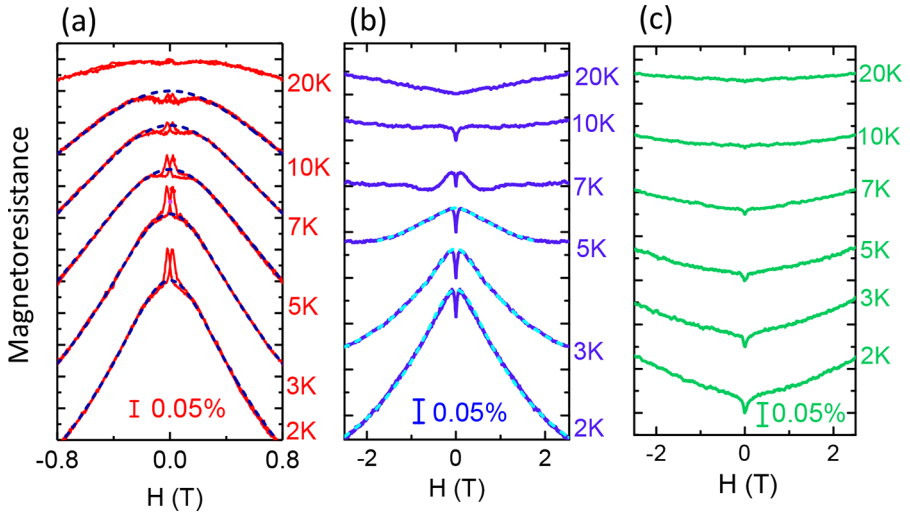


**Figure 5.** MR of (a) EuO/KTO, (b) EuO/STO(5 $\mu$c)/LSAT, and (c) EuO/STO(20 $\mu$c)/LSAT, obtained by cycling the parallel magnetic field in wide ranges. Two processes can be clear seen, taking place in a narrow and a broad field ranges, respectively. Solid lines are experimental data, and the dashed lines are results of curve fitting. For clarity, the MR–$H$ curves corresponding to different temperatures are upward shifted.

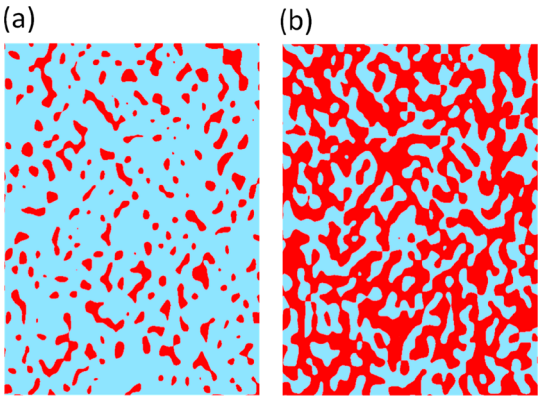


**Figure 6.** Sketches for magnetic structure in the interfacial layer of the quantum well. Plane views of the interfacial layers of KTO and STO with (a) low and (b) high carrier densities. Magnetic clusters (domains) are marked by red areas, while the background with isolated magnetic moments is represented by a gray area.

reported, itinerant electrons can generate a magnetic interaction between magnetic moments in 2DEG.[39] This implies that the magnetic order near interface will be delivered to inner STO layers by mobile electrons. In this scenario, we can understand the appearance of ferromagnetic order in the quantum well.

## 4. CONCLUSIONS

In summary, 2DEGs are obtained by coherently growing NaCl-structured EuO on perovskite $SrTiO_3$. Quantum wells thus obtained have a long-range magnetic order and more conductive magnetic domain walls in the $SrTiO_3$ layers where 2DEG reside, exhibiting isotropic butterfly shaped magnetoresistance and remarkable anomalous Hall effect. The density of mobile electrons is the key factor affecting interfacial magnetism. Through tuning carrier density we are able to control the transition between magnetic states with short-range and long-range orders, respectively. On the basis of experimental results, a magnetic map is obtained for the interfacial layer. The present work demonstrates how to get and tune interfacial magnetism, giving a guidance for the design of high-performance magnetic 2DEG.

## ASSOCIATED CONTENT

### Supporting Information

The Supporting Information is available free of charge at https://pubs.acs.org/doi/10.1021/acsami.0c05332.

Figures of reflection high-energy electron diffraction patterns, temperature-dependent resistance, magnetic field-dependent magnetizations, magnetoresistance fitting, schematic of superlattices, and orbital-projected density of states, tables of fitting parameters and calculated magnetic moments, and discussions of density-functional theory (DFT) calculations (PDF)

## AUTHOR INFORMATION

### Corresponding Author

**Jirong Sun** – *Beijing National Laboratory for Condensed Matter Physics and Institute of Physics, Chinese Academy of Sciences, Beijing 100190, People's Republic of China; School of Physical Sciences, University of Chinese Academy of Sciences, Beijing 100049, People's Republic of China; Songshan Lake Materials Laboratory, Dongguan, Guangdong 523808, People's Republic of China;* orcid.org/0000-0003-1238-8770; Email: jrsun@iphy.ac.cn

### Authors

**Jine Zhang** – *Beijing National Laboratory for Condensed Matter Physics and Institute of Physics, Chinese Academy of Sciences, Beijing 100190, People's Republic of China; School of Physical Sciences, University of Chinese Academy of Sciences, Beijing 100049, People's Republic of China;* orcid.org/0000-0001-7949-3239

**Hui Zhang** – *Fert Beijing Institute, School of Microelectronics, Beijing Advanced Innovation Center for Big Data and Brain Computing, Beihang University, Beijing 100191, People's Republic of China*

**Hongrui Zhang** – *Beijing National Laboratory for Condensed Matter Physics and Institute of Physics, Chinese Academy of Sciences, Beijing 100190, People's Republic of China; School of Physical Sciences, University of Chinese Academy of Sciences, Beijing 100049, People's Republic of China*



https://dx.doi.org/10.1021/acsami.0c05332
ACS Appl. Mater. Interfaces 2020, 12, 28775–28782

**Yang Ma** − *International Centre for Quantum Materials, School of Physics, Peking University, Beijing 100871, People's Republic of China; Collaborative Innovation Centre of Quantum Matter, Beijing 100871, People's Republic of China*

**Xiaobing Chen** − *Beijing National Laboratory for Condensed Matter Physics and Institute of Physics, Chinese Academy of Sciences, Beijing 100190, People's Republic of China; School of Physical Sciences, University of Chinese Academy of Sciences, Beijing 100049, People's Republic of China;* orcid.org/0000-0003-4327-1209

**Fanqi Meng** − *Beijing National Laboratory for Condensed Matter Physics and Institute of Physics, Chinese Academy of Sciences, Beijing 100190, People's Republic of China*

**Shaojin Qi** − *Beijing National Laboratory for Condensed Matter Physics and Institute of Physics, Chinese Academy of Sciences, Beijing 100190, People's Republic of China; School of Physical Sciences, University of Chinese Academy of Sciences, Beijing 100049, People's Republic of China*

**Yuansha Chen** − *Beijing National Laboratory for Condensed Matter Physics and Institute of Physics, Chinese Academy of Sciences, Beijing 100190, People's Republic of China*

**Fengxia Hu** − *Beijing National Laboratory for Condensed Matter Physics and Institute of Physics, Chinese Academy of Sciences, Beijing 100190, People's Republic of China; School of Physical Sciences, University of Chinese Academy of Sciences, Beijing 100049, People's Republic of China; Songshan Lake Materials Laboratory, Dongguan, Guangdong 523808, People's Republic of China*

**Qinghua Zhang** − *Beijing National Laboratory for Condensed Matter Physics and Institute of Physics, Chinese Academy of Sciences, Beijing 100190, People's Republic of China*

**Banggui Liu** − *Beijing National Laboratory for Condensed Matter Physics and Institute of Physics, Chinese Academy of Sciences, Beijing 100190, People's Republic of China; School of Physical Sciences, University of Chinese Academy of Sciences, Beijing 100049, People's Republic of China;* orcid.org/0000-0002-6030-6680

**Baogen Shen** − *Beijing National Laboratory for Condensed Matter Physics and Institute of Physics, Chinese Academy of Sciences, Beijing 100190, People's Republic of China; School of Physical Sciences, University of Chinese Academy of Sciences, Beijing 100049, People's Republic of China; Songshan Lake Materials Laboratory, Dongguan, Guangdong 523808, People's Republic of China*

**Weisheng Zhao** − *Fert Beijing Institute, School of Microelectronics, Beijing Advanced Innovation Center for Big Data and Brain Computing, Beihang University, Beijing 100191, People's Republic of China*

**Wei Han** − *International Centre for Quantum Materials, School of Physics, Peking University, Beijing 100871, People's Republic of China; Collaborative Innovation Centre of Quantum Matter, Beijing 100871, People's Republic of China;* orcid.org/0000-0002-1757-4479

Complete contact information is available at: https://pubs.acs.org/10.1021/acsami.0c05332

### Author Contributions

▲J.Z., Hui Z., Hongrui Z., and Y.M. contributed equally to this work.

### Notes

The authors declare no competing financial interest.

## ■ ACKNOWLEDGMENTS

This work has been supported by the National Basic Research of China (Nos. 2016YFA0300701, 2019YFA0308401, 2018YFA0305704, 2017YFA0303601, 2017YFA0206300, and 2019YFA0704904), the National Natural Science Foundation of China (Nos. 11520101002, 111921004, 11934016, 11974025, 51972335, 51590880, and 11674378), and the Key Program of the Chinese Academy of Sciences.

## ■ REFERENCES

(1) Reyren, N.; Thiel, S.; Caviglia, A. D.; Kourkoutis, L. F.; Hammerl, G.; Richter, C.; Schneider, C. W.; Kopp, T.; Ruetschi, A. S.; Jaccard, D.; Gabay, M.; Muller, D. A.; Triscone, J. M.; Mannhart, J. Superconducting Interfaces between Insulating Oxides. *Science* **2007**, *317*, 1196−1199.

(2) Herranz, G.; Singh, G.; Bergeal, N.; Jouan, A.; Lesueur, J.; Gazquez, J.; Varela, M.; Scigaj, M.; Dix, N.; Sanchez, F.; Fontcuberta, J. Engineering Two-Dimensional Superconductivity and Rashba Spin-Orbit Coupling in $LaAlO_3/SrTiO_3$ Quantum Wells by Selective Orbital Occupancy. *Nat. Commun.* **2015**, *6*, 6028.

(3) Brinkman, A.; Huijben, M.; Van Zalk, M.; Huijben, J.; Zeitler, U.; Maan, J. C.; Van der Wiel, W. G.; Rijnders, G.; Blank, D. H. A.; Hilgenkamp, H. Magnetic Effects at the Interface between Non-Magnetic Oxides. *Nat. Mater.* **2007**, *6*, 493−496.

(4) Lee, J.-S.; Xie, Y. W.; Sato, H. K.; Bell, C.; Hikita, Y.; Hwang, H. Y.; Kao, C.-C. Titanium $d_{xy}$ ferromagnetism at the $LaAlO_3/SrTiO_3$ interface. *Nat. Mater.* **2013**, *12*, 703−706.

(5) Caviglia, A. D.; Gabay, M.; Gariglio, S.; Reyren, N.; Cancellieri, C.; Triscone, J. M. Tunable Rashba Spin-Orbit Interaction at Oxide Interfaces. *Phys. Rev. Lett.* **2010**, *104*, 126803.

(6) Cheng, L.; Wei, L.; Liang, H.; Yan, Y.; Cheng, G.; Lv, M.; Lin, T.; Kang, T.; Yu, G.; Chu, J.; Zhang, Z.; Zeng, C. Optical Manipulation of Rashba Spin−Orbit Coupling at $SrTiO_3$-Based Oxide Interfaces. *Nano Lett.* **2017**, *17*, 6534−6539.

(7) Lesne, E.; Fu, Y.; Oyarzun, S.; Rojas-Sanchez, J. C.; Vaz, D. C.; Naganuma, H.; Sicoli, G.; Attane, J. P.; Jamet, M.; Jacquet, E.; George, J. M.; Barthelemy, A.; Jaffres, H.; Fert, A.; Bibes, M.; Vila, L. Highly Efficient and Tunable Spin-to-Charge Conversion through Rashba Coupling at Oxide Interfaces. *Nat. Mater.* **2016**, *15*, 1261−1266.

(8) Song, Q.; Zhang, H.; Su, T.; Yuan, W.; Chen, Y.; Xing, W.; Shi, J.; Sun, J.; Han, W. Observation of Inverse Edelstein Effect in Rashba-Split 2DEG between $SrTiO_3$ and $LaAlO_3$ at Room Temperature. *Science advances* **2017**, *3*, No. e1602312.

(9) Wang, Y.; Ramaswamy, R.; Motapothula, M.; Narayanapillai, K.; Zhu, D.; Yu, Y.; Venkatesan, T.; Yang, H. Room-Temperature Giant Charge-to-Spin Conversion at the $SrTiO_3$−$LaAlO_3$ Oxide Interface. *Nano Lett.* **2017**, *17*, 7659−7664.

(10) Ben Shalom, M.; Ron, A.; Palevski, A.; Dagan, Y. Shubnikov−De Haas Oscillations in $SrTiO_3/LaAlO_3$ Interface. *Phys. Rev. Lett.* **2010**, *105*, 206401.

(11) Caviglia, A. D.; Gariglio, S.; Cancellieri, C.; Sacépé, B.; Fête, A.; Reyren, N.; Gabay, M.; Morpurgo, A. F.; Triscone, J.-M. Two-Dimensional Quantum Oscillations of the Conductance at $LaAlO_3/SrTiO_3$ Interfaces. *Phys. Rev. Lett.* **2010**, *105*, 236802.

(12) McCollam, A.; Wenderich, S.; Kruize, M. K.; Guduru, V. K.; Molegraaf, H. J. A.; Huijben, M.; Koster, G.; Blank, D. H. A.; Rijnders, G.; Brinkman, A.; Hilgenkamp, H.; Zeitler, U.; Maan, J. C. Quantum oscillations and subband properties of the two-dimensional electron gas at the $LaAlO_3/SrTiO_3$ interface. *APL Mater.* **2014**, *2*, No. 022102.

(13) Xie, Y.; Bell, C.; Kim, M.; Inoue, H.; Hikita, Y.; Hwang, H. Y. Quantum longitudinal and Hall transport at the $LaAlO_3/SrTiO_3$ interface at low electron densities. *Solid State Commun.* **2014**, *197*, 25−29.

(14) Trier, F.; Prawiroatmodjo, G. E. D. K.; Zhong, Z. C.; Christensen, D. V.; von Soosten, M.; Bhowmik, A.; Lastra, J. M. G.; Chen, Y. Z.; Jespersen, T. S.; Pryds, N. Quantization of Hall Resistance at the Metallic Interface between an Oxide Insulator and $SrTiO_3$. *Phys. Rev. Lett.* **2016**, *117*, No. 096804.

(15) Stornaiuolo, D.; Cantoni, C.; De Luca, G. M.; Di Capua, R.; Di Gennaro, E.; Ghiringhelli, G.; Jouault, B.; Marre, D.; Massarotti, D.; Miletto Granozio, F.; Pallecchi, I.; Piamonteze, C.; Rusponi, S.; Tafuri, F.; Salluzzo, M. Tunable Spin Polarization and Superconductivity in Engineered Oxide Interfaces. *Nat. Mater.* **2016**, *15*, 278−284.
(16) Salluzzo, M.; Gariglio, S.; Stornaiuolo, D.; Sessi, V.; Rusponi, S.; Piamonteze, C.; De Luca, G. M.; Minola, M.; Marré, D.; Gadaleta, A.; Brune, H.; Nolting, F.; Brookes, N. B.; Ghiringhelli, G. Origin of Interface Magnetism in $BiMnO_3/SrTiO_3$ and $LaAlO_3/SrTiO_3$ Heterostructures. *Phys. Rev. Lett.* **2013**, *111*, No. 087204.
(17) Gray, M. T.; Sanders, T. D.; Jenkins, C. A.; Shafer, P.; Arenholz, E.; Suzuki, Y. Electronic and Magnetic Phenomena at the Interface of $LaAlO_3$ and Ru Doped $SrTiO_3$. *Appl. Phys. Lett.* **2015**, *107*, 241603.
(18) Gunkel, F.; Bell, C.; Inoue, H.; Kim, B.; Swartz, A. G.; Merz, T. A.; Hikita, Y.; Harashima, S.; Sato, H. K.; Minohara, M.; Hwang, H. Y.; et al. Defect Control of Conventional and Anomalous Electron Transport at Complex Oxide Interfaces. *Phys. Rev. X* **2016**, *6*, No. 031035.
(19) Zhou, H. D.; Goodenough, J. B. Localized or Itinerant $TiO_3$ Electrons in $RTiO_3$ Perovskites. *J. Phys.: Condens. Matter* **2005**, *17*, 7395−7406.
(20) Moetakef, P.; Williams, J. R.; Ouellette, D. G.; Kajdos, A. P.; Goldhaber-Gordon, D.; Allen, S. J.; Stemmer, S. Carrier-Controlled Ferromagnetism in $SrTiO_3$. *Phys. Rev. X* **2012**, *2*, No. 021014.
(21) Biscaras, J.; Bergeal, N.; Kushwaha, A.; Wolf, T.; Rastogi, A.; Budhani, R. C.; Lesueur, J. Two-dimensional Superconductivity at a Mott Insulator/Band Insulator Interface $LaTiO_3/SrTiO_3$. *Nat. Commun.* **2010**, *1*, 89.
(22) Xu, P.; Ayino, Y.; Cheng, C.; Pribiag, V. S.; Comes, R. B.; Sushko, P. V.; Chambers, S. A.; Jalan, B. Predictive Control over Charge Density in the Two-Dimensional Electron Gas at the Polar-Nonpolar $NdTiO_3/SrTiO_3$ Interface. *Phys. Rev. Lett.* **2016**, *117*, 116803.
(23) Ahadi, K.; Stemmer, S. Novel Metal-Insulator Transition at the $SmTiO_3/SrTiO_3$ Interface. *Phys. Rev. Lett.* **2017**, *118*, 236803.
(24) Chen, Y. Z.; Trier, F.; Wijnands, T.; Green, R. J.; Gauquelin, N.; Egoavil, R.; Christensen, D. V.; Koster, G.; Huijben, M.; Bovet, N.; Macke, S.; He, F.; Sutarto, R.; Andersen, N. H.; Sulpizio, J. A.; Honig, M.; Prawiroatmodjo, G. E. D. K.; Jespersen, T. S.; Linderoth, S.; Ilani, S.; Verbeeck, J.; Van Tendeloo, G.; Rijnders, G.; Sawatzky, G. A.; Pryds, N. Extreme Mobility Enhancement of Two Dimensional Electron gases at Oxide Interfaces by Charge-Transfer-Induced Modulation Doping. *Nat. Mater.* **2015**, *14*, 801−807.
(25) Zhang, H. R.; Yun, Y.; Zhang, X. J.; Zhang, H.; Ma, Y.; Yan, X.; Wang, F.; Li, G.; Li, R.; Khan, T.; Chen, Y. S.; Liu, W.; Hu, F. X.; Liu, B. G.; Shen, B. G.; Han, W.; Sun, J. R. High-Mobility Spin-Polarized Two-Dimensional Electron Gases at $EuO/KTaO_3$ Interfaces. *Phys. Rev. Lett.* **2018**, *121*, 116803.
(26) Kormondy, K. J.; Gao, L. Y.; Li, X.; Lu, S. R.; Posadas, A. B.; Shen, S. D.; Tsoi, M.; McCartney, M. R.; Smith, D. J.; Zhou, J. S.; Lev, L. L.; Husanu, M. A.; Strocov, V. N.; Demkov, A. A. Large positive linear magnetoresistance in the two-dimensional $t_{2g}$ electron gas at the $EuO/SrTiO_3$ interface. *Sci. Rep.* **2018**, *8*, 7721.
(27) Ohtomo, A.; Muller, D. A.; Grazul, J. L.; Hwang, H. Artificial charge-modulation in atomic-scale perovskite titanate superlattices. *Nature* **2002**, *419*, 378−380.
(28) Cao, Y.; Yang, Z.; Kareev, M.; Liu, X.; Meyers, D.; Middey, S.; Choudhury, D.; Shafer, P.; Guo, J.; Freeland, J. W.; Arenholz, E.; Gu, L.; Chakhalian, J. Magnetic Interactions at the Nanoscale in Trilayer Titanates. *Phys. Rev. Lett.* **2016**, *116*, No. 076802.
(29) Das, S.; Rastogi, A.; Wu, L. J.; Zheng, J.-C.; Hossain, Z.; Zhu, Y. M.; Budhani, R. C. Kondo scattering in $\delta$-doped $LaTiO_3/SrTiO_3$ interfaces: Renormalization by spin-orbit interactions. *Phys. Rev. B: Condens. Matter Mater. Phys.* **2014**, *90*, No. 081107.
(30) Garcia-Barriocanal, J.; Bruno, F. Y.; Rivera-Calzada, A.; Sefrioui, Z.; Nemes, N. M.; Garcia-Hernández, M.; Rubio-Zuazo, J.; Castro, G. R.; Varela, M.; Pennycook, S. J.; Leon, C.; Santamaria, J. charge leakage" at $LaMnO_3/SrTiO_3$ interfaces. *Adv. Mater.* **2010**, *22*, 627−632.
(31) Jang, H. W.; Felker, D. A.; Bark, C. W.; Wang, Y.; Niranjan, M. K.; Nelson, C. T.; Zhang, Y.; Su, D.; Folkman, C. M.; Baek, S. H.; Lee, S.; Janicka, K.; Zhu, Y.; Pan, X. Q.; Fong, D. D.; Tsymbal, E. Y.; Rzchowski, M. S.; Eom, C. B. Metallic and insulating oxide interfaces controlled by electronic correlations. *Science* **2011**, *331*, 886−889.
(32) Chen, Y. Z.; Bovet, N.; Trier, F.; Christensen, D. V.; Qu, F. M.; Andersen, N. H.; Kasama, T.; Zhang, W.; Giraud, R.; Dufouleur, J.; Jespersen, T. S.; Sun, J. R.; Smith, A.; Nygard, J.; Lu, L.; Büchner, B.; Shen, B. G.; Linderoth, S.; Pryds, N. A high-mobility two-dimensional electron gas at the spinel/perovskite interface of $\gamma$-$Al_2O_3/SrTiO_3$. *Nat. Commun.* **2013**, *4*, 1371.
(33) Xiao, X.; Li, J. X.; Ding, Z.; Wu, Y. Z. Four-fold symmetric anisotropic magnetoresistance of single-crystalline Ni (001) film. *J. Appl. Phys.* **2015**, *118*, 203905.
(34) Ohandley, R. C. *Modern Magnetic Materials*; John Wiley & Sons, Inc., 2000; pp 573−579.
(35) Xiao, J. Q.; Jiang, J. S.; Chien, C. L. Giant Magnetoresistance in Nonmultilayer Magnetic Systems. *Phys. Rev. Lett.* **1992**, *68*, 3749−3752.
(36) Roßler, S.; Ernst, S.; Padmanabhan, B.; Elizabeth, S.; Bhat, H. L.; Steglich, F.; Wirth, S. Nanometer-scale phase separation in a colossal magnetoresistive Manganite. *EPL* **2008**, *83*, 17009.
(37) Hwang, H. Y.; Cheong, S.-W.; Ong, N. P.; Batlogg, B. Spin-Polarized Intergrain Tunneling in $La_{2/3}Sr_{1/3}MnO_3$. *Phys. Rev. Lett.* **1996**, *77*, 2041−2044.
(38) Minhas, M. Z.; Müller, A.; Heyroth, F.; Blaschek, H. H.; Schmidt, G. Temperature Dependent Giant Resistance Anomaly in $LaAlO_3/SrTiO_3$ Nanostructures. *Sci. Rep.* **2017**, *7*, 5215.
(39) Joshua, A.; Ruhman, J.; Pecker, S.; Altman, E.; Ilani, S. Gate-Tunable Polarized Phase of Two-Dimensional Electrons at the $LaAlO_3/SrTiO_3$ Interface. *Proc. Natl. Acad. Sci. U. S. A.* **2013**, *110*, 9633−9638.
(40) Stöhr, J.; Siegmann, H. C. *Magnetism*; Springer: Berlin, Germany, 2006; pp 290−292.
(41) Ohtomo, A.; Hwang, H. Y. A High-Mobility Electron Gas at the $LaAlO_3/SrTiO_3$ Heterointerface. *Nature* **2004**, *427*, 423−426.
(42) Zhang, H.; Zhang, H. R.; Yan, X.; Zhang, X. J.; Zhang, Q. H.; Zhang, J.; Han, F. R.; Gu, L.; Liu, B. G.; Chen, Y. S.; Shen, B. G.; Sun, J. R. Highly Mobile Two-Dimensional Electron Gases with a Strong Gating Effect at the Amorphous $LaAlO_3/KTaO_3$ Interface. *ACS Appl. Mater. Interfaces* **2017**, *9*, 36456−36461.
(43) Khosla, R. P.; Fischer, J. R. Magnetoresistance in Degenerate Cds: Localized Magnetic Moments. *Phys. Rev. B* **1970**, *2*, 4084−4097.
(44) Modepalli, V.; Jin, M. J.; Park, J.; Jo, J.; Kim, J. H.; Baik, J. M.; Seo, C.; Kim, J.; Yoo, J. W. Gate-Tunable Spin Exchange Interactions and Inversion of Magnetoresistance in Single Ferromagnetic ZnO Nanowires. *ACS Nano* **2016**, *10*, 4618−4626.
(45) Zhang, H. R.; Yan, X.; Zhang, H.; Wang, F.; Gu, Y.; Ning, X.; Khan, T.; Li, R.; Chen, Y. S.; Liu, W.; Wang, S.; Shen, B. G.; Sun, J. R. Magnetic Two-Dimensional Electron Gases with High Curie Temperatures at $LaAlO_3/SrTiO_3$:Fe Interfaces. *Phys. Rev. B: Condens. Matter Mater. Phys.* **2018**, *97*, 155150.
(46) Zeng, Y. J.; Pereira, L. M.; Menghini, M.; Temst, K.; Vantomme, A.; Locquet, J. P.; Van Haesendonck, C. Tuning Quantum Corrections and Magnetoresistance in ZnO Nanowires by Ion Implantation. *Nano Lett.* **2012**, *12*, 666−672.
(47) Schoonus, J. J. H. M.; Bloom, F. L.; Wagemans, W.; Swagten, H. J. M.; Koopmans, B. Extremely Large Magnetoresistance in Boron-Doped Silicon. *Phys. Rev. Lett.* **2008**, *100*, 127202.


https://dx.doi.org/10.1021/acsami.0c05332
*ACS Appl. Mater. Interfaces* 2020, 12, 28775−28782